Single-Site Heterogeneous Organometallic Ir Catalysts Embedded on Graphdiyne: Structural Manipulation Beyond the Carbon Support

HPSTAR
1532-2022

Hong Liu, Haiyuan Zou, Mei Wang, Hongliang Dong, Dan Wang, Fan Li, Hao Dai, Tao Song, Shuting Wei, Yongfei Ji,* Chenguang Wang,* and Lele Duan*

Accurate control over the coordination circumstances of single-atom catalysts (SACs) is decisive to their intrinsic activity. Here, two single-site heterogeneous organometallic catalysts (SHOCs), Cp*Ir–L/GDY (L = OH− and Cl−; Cp* = pentamethylcyclopentadienyl), with the fine-tuned local coordination and electronic structure of Ir sites, are constructed by anchoring Cp*Ir complexes on graphdiyne (GDY) matrix via a one-pot procedure. The spectroscopic studies and theoretical calculations indicate that the Ir atoms in Cp*Ir–Cl/GDY and Cp*Ir–OH/GDY have a much higher oxidation state than Ir in the SAC Ir/GDY. As a proof-of-principle demonstration, the GDY-supported SHOCs are used for formic acid dehydrogenation, which display a fivefold enhancement of catalytic activity compared with SAC Ir/GDY. The kinetic isotope effect and in situ Fourier-transform infrared studies reveal that the rate-limiting step is the β-hydride elimination process, and Cp* on the Ir site accelerates the β-hydride elimination reaction. The GDY-supported SHOCs integrate the merits of both SACs and molecular catalysts, wherein the isolated Ir anchored on GDY echoes with SACs' behavior, and the Cp* ligand enables precise structural and electronic regulation like molecular catalysts. The scheme of SHOCs adds a degree of freedom in accurate regulation of the local structure, the electronic property, and therefore the catalytic performance of single-atom catalysts.

1. Introduction

The heterogeneous single-atom catalysts (SACs) have been extensively studied for energy conversion, chemical transformation, and environmental remediation.[1] The SACs feature the atomically-dispersed active sites which are immobilized on given support through covalent coordination or ionic interaction, hence allowing for maximal active-site utilization. By fine-tuning the interaction between the anchored single sites and their neighboring surface atoms, the electronic property and catalytic activity of SACs could be optimized in principle. In this respect, SACs build a bridge between homogeneous and heterogeneous catalysts.

Despite the significant progress achieved in the construction of various SACs, limited attempts have been made to exquisitely regulate the local coordination structure of SACs,[2] mainly due to the lack of practical synthetic approaches for precisely tailoring the coordination sphere of SACs, especially for those supported on carbon materials. For instance, the widely documented SACs of atomic metal–nitrogen–carbon moieties[3] on carbon substrates are usually synthesized by pyrolysis at high-temperature. Such a condition is too extreme to fine-tune the local coordination sphere of the catalytically active metal centers, posing a challenge for modulating the configuration at an atomic/molecular level.[4] Thus, synthetic strategies are required to add another degree of freedom to tune the metal centers in a molecular way, where the active sites can be feasibly and flexibly tailored. Drop-casting the molecular catalysts on heterogeneous support, to some extent, ensures fine-tuned active site by utilizing the inherent coordination environment of molecular catalysts, while catalysts are prone to aggregate

H. Liu, M. Wang
State Key Laboratory of Fine Chemicals
Dalian University of Technology
Dalian 116024, P. R. China
H. Liu, H. Zou, D. Wang, F. Li, H. Dai, T. Song, S. Wei, L. Duan
Department of Chemistry
Shenzhen Grubbs Institute
Southern University of Science and Technology
Shenzhen 518055, P. R. China
E-mail: duanll@sustech.edu.cn

The ORCID identification number(s) for the author(s) of this article can be found under https://doi.org/10.1002/smll.202203442.

H. Dong
Center for High-Pressure Science and Technology Advanced Research
Pudong, Shanghai 201203, P. R. China
Y. Ji
School of Chemistry and Chemical Engineering
Guangzhou University
Guangzhou, Guangdong 510006, P. R. China
E-mail: yongfeiji2018@gzhu.edu.cn
C. Wang
Guangzhou Institute of Energy Conversion
Chinese Academy of Sciences
Guangzhou 510075, P. R. China
E-mail: wangcg@ms.giec.ac.cn

ADVANCED
SCIENCE NEWS
www.advancedsciencenews.com

NANO · MICRO
small
www.small-journal.com

and suffer from serious leaching issues under catalytic conditions.[5] As an extension of this approach, attaching molecular catalysts on the support through covalent bonds circumvents these problems but needs functional groups on both molecular catalysts and the supporting materials to realize the covalent connection. As a result, this approach is tedious and may alter the electronic structure of the molecular catalysts.[6] A remedy to this troublesome approach is anchoring organometallic catalysts to carbon materials in the form of SACs to construct the expected single-site heterogeneous organometallic catalysts (SHOCs; note that the organometallic motifs of SHOCs are immobilized on both external and internal surfaces of the layered materials, making SHOCs different from the well-known surface organometallic catalysts where the organometallic motifs are bound to the external surface of supporting materials),[7] which are endowed not only with the desired features of SACs but also with the merits of molecular catalysts. This synthetic strategy allows the structural manipulation of SACs beyond the carbon supports.

Herein, we report two Cp*Ir-based SHOCs anchored on the graphdiyne (GDY) matrix, which were constructed through a one-pot synthetic strategy. As a 2D carbon allotrope, GDY is periodically constituted by the sp- and sp^2-hybridized carbon atoms.[8] The ordered 18 C-hexagonal pores on the GDY, formed by three butadiyne linkages between the benzene rings, provide ideal coordinating sites for immobilization of single atoms.[9] Very recently, our group has reported a versatile synthetic procedure using high-valence metal salts and hexaethynylbenzene (HEB) to deposit various metal single-atoms on the GDY matrix.[10] In this work, the deployed Cp*Ir molecular catalysts are capable of driving the cross-coupling reaction of GDY monomers, and meanwhile the Cp*Ir molecular catalysts could be simultaneously confined and chelated on the porous GDY framework, leading to the formation of isolated molecular-sites as Cp*Ir/GDY moieties (**Figure 1**). To our delight, the prepared SHOCs integrate the merits of both SACs and molecular catalysts, where the atomic Ir sites are stabilized by the GDY matrix, and their electronic property is exquisitely tuned by the inherent Cp* ligand. Formic acid (FA) dehydrogenation, which is considered a promising strategy for on-site hydrogen evolution,[11] was used as a model reaction to elucidate the structure–function relationship of the as-synthesized SHOCs. Benefitted from the electronic-regulating ability of Cp*, the turnover frequency (TOF) on the optimum Cp*Ir SHOCs is six times as high as that of Ir SACs. The scheme of SHOCs provides a practical way to accurately regulate the local coordination and electronic property, and therefore the catalytic performance of atomically dispersed active sites. In principle, such a one-pot synthetic strategy adds a degree of freedom for catalyst design and paves the way to expanding the scope of SACs on carbon materials.

2. Results and Discussion

2.1. Synthesis

The schematic illustration of the one-pot synthetic strategy for target Ir catalysts is depicted in Figure 1. The monomer HEB was prepared from hexakis[(trimethylsilyl)ethynyl]benzene by
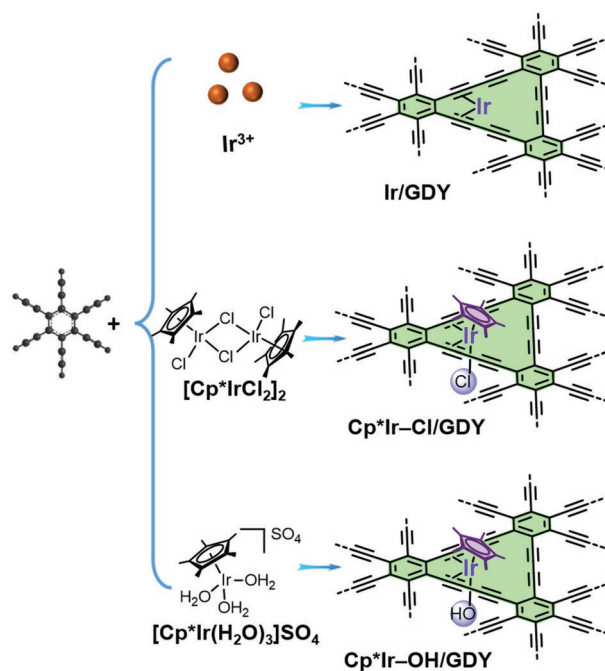

Figure 1. Schematic of the synthetic procedure for Ir/GDY, Cp*Ir–Cl/GDY, and Cp*Ir–OH/GDY.

desilylation[8a] and then used immediately for the coupling reaction, in which HEB was mixed with an iridium precursor, such as IrCl$_3$, [Cp*IrCl$_2$]$_2$, and [Cp*Ir(H$_2$O)$_3$]SO$_4$, in pyridine under argon atmosphere. The monomer HEB underwent oxidative coupling to form the C—C bond in the presence of high-valence iridium precursors, and these iridium precursors were concomitantly reduced to low-valent metal species. Moreover, the in situ formed GDY provided abundant coordination sites to stabilize the reduced iridium species. Consequently, densely atomic/molecular Ir sites were dispersed on the GDY matrix, and the resulting materials are denoted as Ir/GDY, Cp*Ir–Cl/GDY, and Cp*Ir–OH/GDY (see their structures in Figure 1).

2.2. Morphology

The morphology of as-prepared materials was characterized by bright field transmission electron microscopy (BF-TEM) and aberration-corrected high-angle annular dark-field scanning transmission electron microscopy (HAADF-STEM). The BF-TEM images show an aggregated flake-like morphology for all three samples (Figure S1, Supporting Information). Dense atomically dispersed Ir sites but no aggregated Ir particles on GDY were observed by HAADF STEM analysis of different regions of samples (**Figure 2**a–c; and Figure S2, Supporting Information). The Ir sites were clearly identified by numerous separated bright dots under a high-magnification mode. Moreover, the elemental mapping images obtained by energy-dispersive X-ray spectroscopy indicated the uniform distributions of Ir, C, and O elements on Ir/GDY; Ir, C, and Cl elements on Cp*Ir–Cl/GDY; and Ir, C, O, and S elements on Cp*Ir–OH/GDY over the entire architecture (Figure 2d–f; and Figure S3, Supporting Information). The existence of oxygen element on
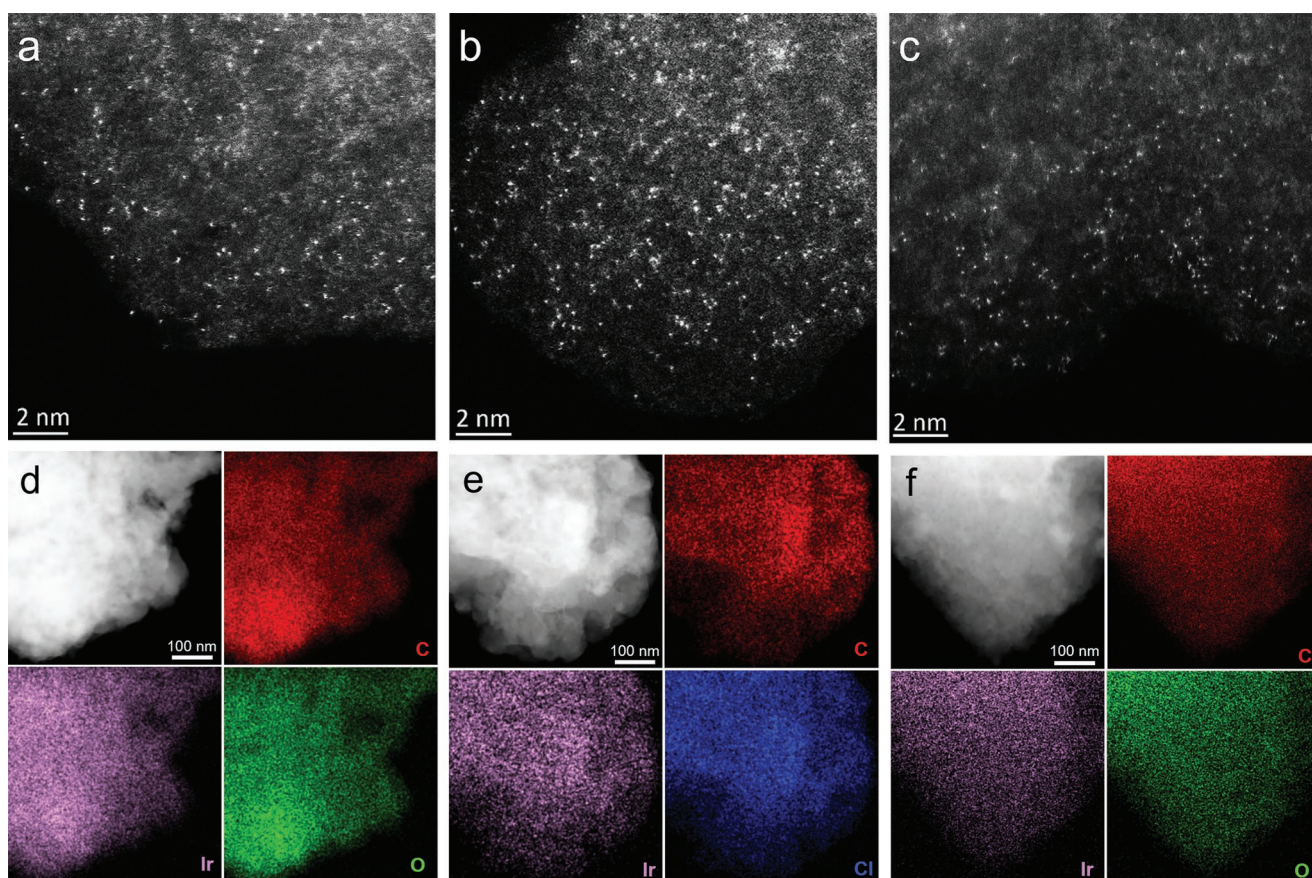
Figure 2. HAADF STEM images of a) Ir/GDY, b) Cp*Ir–Cl/GDY, and c) Cp*Ir–OH/GDY. Dark field STEM images of d) Ir/GDY, e) Cp*Ir–Cl/GDY, and f) Cp*Ir–OH/GDY and the corresponding element mapping images of Ir, C, O, and Cl.

the entire architecture could be explained by the oxygenation of some exposed terminal acetylene groups on the GDY surface. The S mapping image (Figure S4, Supporting Information) shows a fair amount of S element is uniformly distributed on Cp*Ir–OH/GDY, suggesting that some of the SO_4^{2-} ions of $[Cp*Ir(H_2O)_3]SO_4$ remains in the as-prepared material and cannot be washed away. The Ir loadings of 17.51, 15.36, and 9.12 wt% on Cp*Ir–Cl/GDY, Cp*Ir–OH/GDY, and Ir/GDY, respectively, were determined by inductively coupled plasma mass spectrometry (ICP-MS). The loading mass is considerably higher than those reported very recently via the pyrolysis method.[12]

2.3. Spectroscopic Characterization

The Raman spectra of Cp*Ir-Cl/GDY, Cp*Ir-OH/GDY, and Ir/GDY (Figure S5, Supporting Information) are in good agreement with the reported spectrum of GDY.[8a,9c] The minor peaks of as-prepared samples around 2200 cm^{-1} are ascribed to the acetylene bond, and the other two peaks at 1347 and 1552 cm^{-1} correspond to the D and G bands of sp^2 carbons, revealing the successful construction of GDY substrates. The intensity ratios of I_D/I_G are 0.746, 0.743, and 0.701 for Cp*Ir–Cl/GDY, Cp*Ir–OH/GDY, and Ir/GDY, respectively, which indicates that the introduction of Cp*Ir on GDY increases the defects of GDY.

The Fourier-transform infrared (FTIR) spectra of Ir/GDY, Cp*Ir–Cl/GDY, Cp*Ir–OH/GDY, and $[Cp*IrCl_2]_2$ are shown in Figure S6 (Supporting Information). The precursor $[Cp*IrCl_2]_2$ displayed three strong vibration bands at 1450, 1380, and 1029 cm^{-1}, of which the first two bands are assigned to the out-of-plane bending vibration of C−H and the third one to the skeletal vibration of the Cp* ring. All these three characteristic bands were also observed in the FTIR spectra of Cp*Ir–Cl/GDY and Cp*Ir–OH/GDY, but the bands of 1380 and 1029 cm^{-1} were not detected for Ir/GDY although it coincidently displayed a small band at 1450 cm^{-1}. The results evince the successful introduction of Cp*Ir complexes on GDY for both Cp*Ir–Cl/GDY and Cp*Ir–OH/GDY.

The solid-state ^{13}C NMR spectra of Ir/GDY, Cp*Ir–Cl/GDY, and Cp*Ir–OH/GDY were studied to further reveal the coordination structures of the metal centers in as-prepared catalysts (Figure S7, Supporting Information). The peaks at 110–160 ppm represent for the sp^2-hybridized carbons of the benzene and Cp* rings, and the peaks at 75–105 ppm for the sp-hybridized carbons of butadiyne linkers. The sharp peak at 6.5 ppm that is only observed for Cp*Ir–Cl/GDY and Cp*Ir–OH/GDY is attributed to the sp^3-hybridized carbons of the methyl groups of the Cp* fragment.

The weak and broad peaks in the X-ray diffraction (XRD) patterns of Cp*Ir–Cl/GDY, Cp*Ir–OH/GDY, and Ir/GDY indicate the low degree of crystallinity of the samples (Figure S8a,

ADVANCED
SCIENCE NEWS
www.advancedsciencenews.com

NANO · MICRO
small
www.small-journal.com

Supporting Information). Ir/GDY showed a broad peak at 21° in its XRD pattern, which is identical to that indexed to the (002) plane of GDY,[9a] indicating that the insertion of naked single Ir atoms does not apparently influence the interplanar spacing of GDY layers. By contrast to the SAC Ir/GDY, this characteristic peak shifts from 21° to 12° for the SHOCs Cp*Ir–Cl/GDY and Cp*Ir–OH/GDY, signifying the increase of the interplanar spacing of GDY layers (≈7.4 Å) by the insertion of Cp*Ir–L (Figure S8b, Supporting Information). The XRD data also demonstrate that there is no a subset of Ir/GDY in Cp*Ir–Cl/GDY and Cp*Ir–OH/GDY, which means with Cp*Ir complexes as precursors the Cp* ligand will not dissociate from the Ir atom during the preparation process.

The samples were then characterized by X-ray photoelectron spectroscopy (XPS). The C 1s core-level XPS spectra of Ir/GDY (Figure S9, Supporting Information) can be fitted into the peaks at 284.51, 285.22, 286.89, and 288.14 eV, attributing to GDY-based C—C(sp^2), C—C(sp), C—O, and C=O, respectively. By contrast, one more peak at 283.50 eV can be fitted in the C 1s XPS spectra of Cp*Ir–Cl/GDY and Cp*Ir–OH/GDY, which is assigned to the sp^3 carbon of the Cp* ligand. Moreover, the area ratio of sp^2 and sp carbons is close to 1:2 for Ir/GDY, while the area of sp^2 carbons is increased for Cp*Ir–Cl/GDY and Cp*Ir–OH/GDY, which could be attributed to the contribution of sp^2 carbons in the Cp* ring.

All the above spectroscopic characterizations of Cp*Ir–Cl/GDY and Cp*Ir–OH/GDY support the successful grafting the Cp*Ir moieties on GDY. Additionally, compared with the C 1s peaks of GDY, the C 1s spectra of Cp*Ir–Cl/GDY, Cp*Ir–OH/GDY, and Ir/GDY exhibited a new peak at about 290.8 eV due to the π–π* transition arising from the restoration of the delocalized conjugated structure,[9c,d] suggesting the presence of interaction between Cp*Ir (or Ir) and the GDY framework. To further prove the interaction between Cp*Ir and GDY, we synthesized a material, denoted as Cp*Ir–H₂O/GDY, where [Cp*Ir(H₂O)₃]SO₄ was physically absorbed on GDY (note that Cp*Ir–H₂O/GDY was prepared by soaking GDY in a [Cp*Ir(H₂O)₃]SO₄ solution at room temperature). The Ir 4f spectra of Cp*Ir–H₂O/GDY and Cp*Ir–OH/GDY are shown in Figure S10 (Supporting Information). Compared to Cp*Ir–H₂O/GDY, Cp*Ir–OH/GDY displays negatively shifted binding energies of Ir $4f_{5/2}$ and Ir $4f_{7/2}$, suggesting the strong interaction or coordination between Cp*Ir and GDY in the material of Cp*Ir–OH/GDY. More evidence on the coordination between Cp*Ir and GDY for our catalysts was provided based on the extended X-ray absorption fine structure (EXAFS) analysis and density functional theory (DFT) calculations (see below).

2.4. Ligation of Cl⁻ and OH⁻

The ligation of Cl⁻ in Cp*Ir–Cl/GDY is evidenced by the high-resolution Cl 2p XPS spectra (Figure S11a, Supporting Information). To rationally identify the Cl 2p peaks, the Cl 2p XPS spectra of two references, NaCl/GDY (obtained by the physical adsorption of NaCl on GDY, in which free Cl⁻ is present) and [Cp*IrCl₂]₂ (in which Cl⁻ is bound with Ir), were measured, which displayed Cl $2p_{1/2}$/Cl $2p_{3/2}$ peaks at 198.98/197.39 and 201.63/200.04 eV, respectively. The Cl 2p

peaks of Cp*Ir–Cl/GDY could be deconvoluted to two sets at 198.94/197.33 and 201.53/199.95 eV, while only one set of Cl 2p peaks at 198.94/197.36 eV was detected for Ir/GDY. By comparing the spectra of Cp*Ir–Cl/GDY and Ir/GDY with those of the two references, it could be deduced that both bound Cl⁻ (Ir–Cl) and free Cl⁻ exist in Cp*Ir–Cl/GDY, but in Ir/GDY all residual chlorides are free Cl⁻ ions on the GDY framework.

The ligation of OH⁻ in Cp*Ir–OH/GDY is supported by the O 1s XPS spectra (Figure S11b, Supporting Information). The O 1s spectrum of Ir/GDY could be deconvoluted to two peaks at 533.02 and 532.02 eV, corresponding to C—O and C=O units of some oxidized terminal acetylene groups of GDY. Notably, the O 1s spectrum of Cp*Ir–OH/GDY is broader than that of Ir/GDY. It has been documented that the O 1s peaks of metal hydroxides are at around 531.0 eV.[13] Thereby, we proposed that the O 1s spectrum of Cp*Ir–OH/GDY is composed of four peaks at 533.02 (C—O), 532.02 (C=O), 531.31 (SO_4^{2-}) and 530.81 eV (Ir–OH). The assignment of hydroxo ligation is further supported by the DFT calculations. Upon geometry optimizations, the structure of Cp*Ir–OH₂/GDY became unstable and the aqua ligand dissociates from the Ir center. On the other hand, when the water molecule was replaced by the hydroxo ligand, the structure of Cp*Ir–OH/GDY was obtained with a local energy minimum. Accordingly, the structure of Cp*Ir–OH/GDY was proposed.

2.5. Coordination Structure

The local coordination structure around Ir was studied by the EXAFS analysis. **Figure 3**a shows the Fourier transform curves in the R space of the Ir L_3-edge EXAFS spectra for Ir/GDY, Cp*Ir–Cl/GDY, and Cp*Ir–OH/GDY in comparison with the references of Ir foil and IrCl₃. The absence of Ir—Ir bond (≈2.6 Å) verifies that the single-site feature of Ir is achieved over the as-prepared samples. A major peak at ≈1.65 Å was observed for each sample, due to mostly the Ir—C backscattering of the as-prepared samples; this peak was slightly positively shifted (≈1.72 Å) for Cp*Ir–Cl/GDY in comparison with Ir/GDY and Cp*Ir–OH/GDY, which is presumably contributed by the longer Ir—Cl bond of Cp*Ir–Cl/GDY than the Ir—C/O bonds of Ir/GDY and Cp*Ir–OH/GDY. Additionally, the extra peak at ≈1.15 Å for Cp*Ir–OH/GDY should arise from the X-ray scattering in terms of the covalent radius (1.27 Å) of Ir. The wavelet transform (WT) analysis was carried out for discriminating the backscattering atoms and providing an effective resolution in the k and R spaces. The WT EXAFS oscillations of Ir L_3-edge exhibited a sole intensity maximum at ≈6 Å⁻¹, corroborating the atomic dispersion of Ir species on the GDY matrix (Figure 3b). The EXAFS curve-fitting analysis reveals that Cp*Ir–L/GDY (L = Cl⁻, OH⁻) and Ir/GDY moieties are well established (Figure 3a; and Figure S12 and Table S1, Supporting Information). Besides, EXAFS fitting results with various other reference structures are depicted in Figure S13 (Supporting Information). Taking the materials of Cp*Ir–Cl/GDY and Cp*Ir–OH/GDY for instance, if we assumed that the reaction precursors were physically adsorbed on the surface of GDY, the Ir species would exist in the form of precursors. When the crystal structures of precursors were used for fitting,
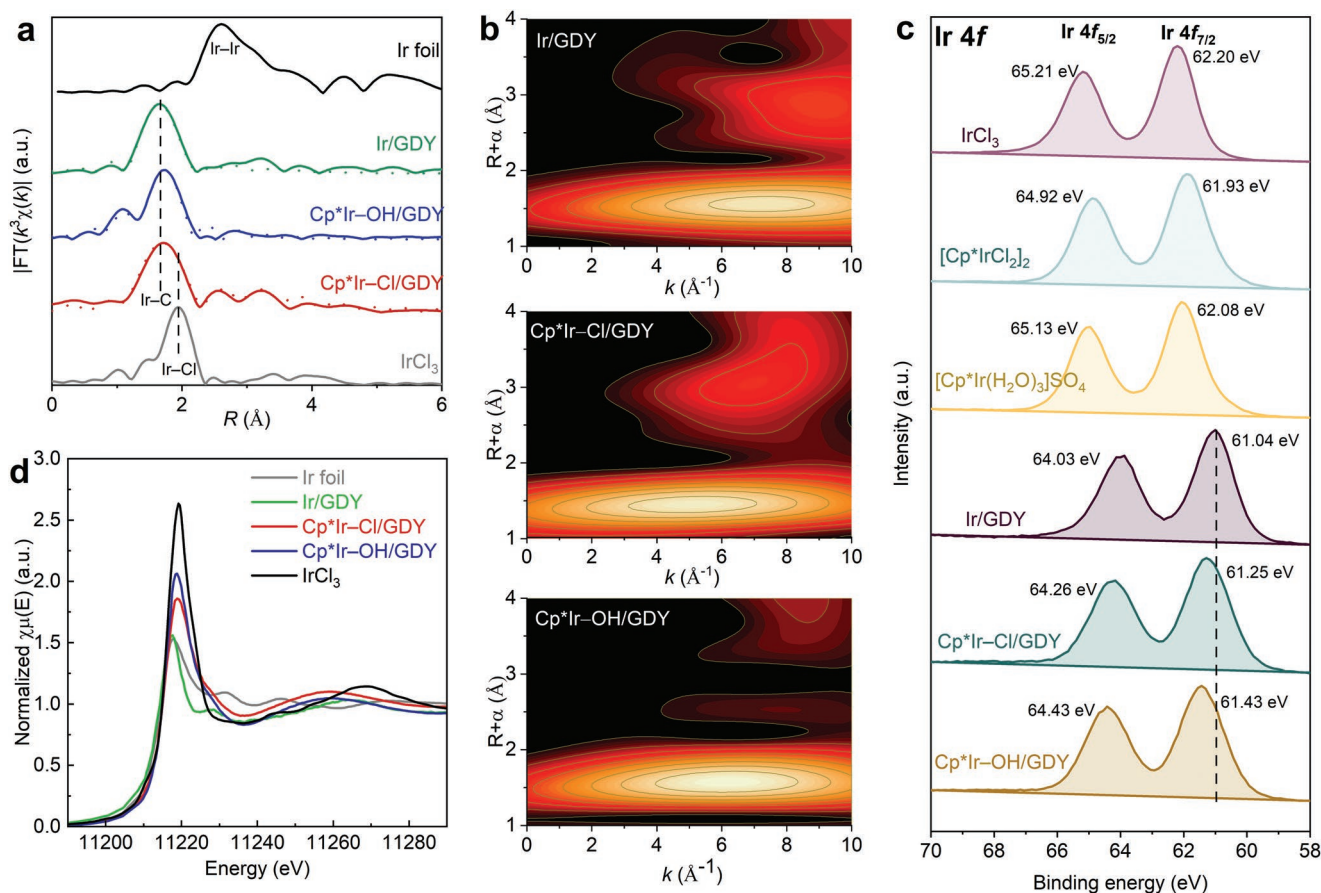
Figure 3. a) EXAFS spectra in R space for Ir/GDY, Cp*Ir–Cl/GDY, Cp*Ir–OH/GDY, Ir foil, and IrCl$_3$ with related fitting curves (dot lines). b) The wavelet transform analysis for Ir/GDY, Cp*Ir–Cl/GDY, and Cp*Ir–OH/GDY. c) High-resolution Ir 4f XPS spectra of Ir/GDY, Cp*Ir–Cl/GDY, Cp*Ir–OH/GDY, and related iridium precursors. d) XANES spectra of Ir/GDY, Cp*Ir–Cl/GDY, Cp*Ir–OH/GDY, Ir foil, and IrCl$_3$ at the Ir L_3-edge.

their fitting curves (Figure S13d,f, Supporting Information) are much worse than those obtained with the proposed structures (Figure S13c,e, Supporting Information). On these premises, single-molecular-site and single-atom Ir configurations were successfully established, which extends the boundary of conventional homogeneous and heterogeneous catalysts. The results from EXAFS studies demonstrated that the organometallic Ir complexes were successfully embedded on the 2D GDY via the metal-support coordinate bonds.

2.6. Electronic Perturbation

To gain insight into the electronic structure of Ir/GDY, Cp*Ir–Cl/GDY, and Cp*Ir–OH/GDY, we measured the high-resolution XPS spectra of Ir 4f orbitals and the synchrotron-based X-ray absorption near-edge structure (XANES) at Ir L_3-edge. The precursors IrCl$_3$, [Cp*IrCl$_2$]$_2$, and [Cp*Ir(H$_2$O)$_3$]SO$_4$ display Ir 4$f_{5/2}$/ Ir 4$f_{7/2}$ peaks at 65.21/62.20, 64.92/61.93, and 65.13/62.08 eV, respectively (Figure 3c). In comparison, the binding energy values of Ir 4f at 64.03/61.04 eV for Ir/GDY, 64.26/61.25 eV for Cp*Ir–Cl/GDY, and 64.43/61.43 eV for Cp*Ir–OH/GDY are significantly shifted to lower binding energy by 1.18, 0.66, and 0.70 eV than that for their corresponding precursors. Moreover,

the Ir binding energies of Cp*Ir–Cl/GDY and Cp*Ir–OH/GDY are higher than Ir/GDY, signifying that the oxidation state of Ir in Cp*Ir–Cl/GDY and Cp*Ir–OH/GDY is higher than that in Ir/GDY.

As shown in Figure 3d, the Ir L_3-edge XANES spectra of as-prepared samples together with references Ir foil and IrCl$_3$ are characterized by broad white lines, which are primarily attributed to the electron transition from occupied 2p to empty 5d states.[12] The Ir L_3-edge white-line intensities of Ir/GDY, Cp*Ir–Cl/GDY, and Cp*Ir–OH/GDY lie between those of the Ir foil and IrCl$_3$, and their intensities increased in the order of Cp*Ir–OH/GDY > Cp*Ir–Cl/GDY > Ir/GDY. The average oxidation states of Ir estimated by the integrated area of the Ir L_3-edge white-line intensity are +1.3 for Cp*Ir–OH/GDY, +0.8 for Cp*Ir–Cl/GDY, and +0.2 for Ir/GDY (Figure S14, Supporting Information). Consistent with the results of inference from Ir 4f XPS spectra, XANES studies also demonstrate that the oxidation state of Ir in Cp*Ir–L/GDY (L = Cl$^-$, OH$^-$) is higher than that in Ir/GDY, most probably because the negatively charged strong electron-donating ligands Cp*/Cl$^-$/HO$^-$ increase the energy level of d-electrons of Ir and thus favor the back-bonding from Ir to the coordinated triple bonds in the GDY matrix.

DFT calculations were performed to examine the Bader charge[14] of the center Ir atoms of Ir/GDY, Cp*Ir–Cl/GDY,

and Cp*Ir–OH/GDY. The results are summarized in Table S2 (Supporting Information). For Ir/GDY, the Bader charge of Ir is +0.36 while it increases to +0.68 for Cp*Ir–Cl/GDY and further to +0.80 for Cp*Ir–OH/GDY. The trend of calculated Bader charges agrees well with that of the oxidation states estimated on the basis of Ir $4f$ XPS and XANES spectra. When Cp*Ir–Cl/GDY and Cp*Ir–OH/GDY are used for FA dehydrogenation, they have to transform in situ to Cp*Ir/GDY by the dissociation of chlorine and hydroxo ligands. Then, Cp*Ir/GDY reacts with formate to yield Cp*Ir–OOCH/GDY, which undergoes multiple reaction steps to achieve FA dehydrogenation. Thereby, we also analyzed the Bader charge of Ir on Cp*Ir/GDY. It's Bader charge is +0.55, just in between those of Ir/GDY and Cp*Ir–Cl/GDY. These results suggest that the ligation of Cp*, Cl^-, and OH^- increases the positive charge on the Ir atom. To understand this phenomenon, we analyzed the differential charge density for Cp*Ir/GDY. The results show that Ir loses electrons while electrons accumulate between Ir and GDY as well as Ir and Cp* (Figure S15, Supporting Information), suggesting that electrons are further transferred from Ir to GDY (and to Cp*) via the formation of polar covalent bonds between them.

2.7. Catalysis

Evidently, the electronic structure of the Ir centers has been modulated by the introduction of the Cp* ligand, and the electronic perturbation would result in an apparent effect on the chemical property of the Ir centers, such as catalytic property. With a view to illustrating such effect, a proof-of-concept test of Ir/GDY, Cp*Ir–Cl/GDY, and Cp*Ir–OH/GDY toward FA dehydrogenation was conducted. The amount of released H_2/CO_2 was monitored by pressure transducers for kinetic studies (Figure S16, Supporting Information), and a wet gas meter was used to record the gas volume for long-term evaluation. Initially, the catalytic activity of Ir-based catalysts was examined in a 3.0 M FA aqueous solution at 363 K. The results are shown in **Figure 4**a,b. Cp*Ir–Cl/GDY and Cp*Ir–OH/GDY displayed evidently higher activity than Ir/GDY. About 4.6 L of gas (mixed H_2 and CO_2 with $H_2:CO_2 = 1:1$; corresponding to 96% conversion) was generated for Cp*Ir–Cl/GDY and Cp*Ir–OH/GDY in ≈19 and 33 h, respectively. In comparison, only 2.7 L of gas (a conversion of 56%) was released for Ir/GDY over an 80 h reaction. Gas chromatography analysis showed that there were H_2 and CO_2 but no CO in the generated gas, indicating an excellent H_2 selectivity of Cp*Ir–OH/GDY, Cp*Ir–Cl/GDY, and Ir/GDY toward the FA dehydrogenation reaction. The initial TOF values (calculated based on the data in the initial 30 min) are 850 h^{-1} for Cp*Ir–OH/GDY, 560 h^{-1} for Cp*Ir–Cl/GDY, and 150 h^{-1} for Ir/GDY. The activity of Cp*Ir–OH/GDY is about 6 times as high as that of Ir/GDY. For comparison, we also examined the catalytic properties of Ir precursors, $[Cp*IrCl_2]_2$ and $[Cp*Ir(H_2O)_3]$ SO_4. The initial TOF values for $[Cp*IrCl_2]_2$ and $[Cp*Ir(H_2O)_3]$ SO_4 are 200 and 330 h^{-1} (Figure 4b), respectively. The catalytic performances of Cp*Ir–Cl/GDY and Cp*Ir–OH/GDY are superior to those of their precursors. Notably, the electronic modulation of Ir single-atom catalysts by Cp* resulted in a significant improvement on the catalytic activity, showing the advantage of our strategy of structural manipulation beyond the carbon support.

To figure out the influence of the Ir loading on the catalytic activity of Cp*Ir-OH/GDY, we modified the Ir loading of Cp*Ir-OH/GDY by changing the amount of precursor in the preparation process and obtained the samples of Cp*Ir–OH/GDY-2 and Cp*Ir–OH/GDY-3. The Ir loadings of 9.31 and 7.59 wt% for these two samples were determined by ICP-MS analysis. The TOF values (based on the data in the initial 30 min) are 930 and 970 h^{-1} for Cp*Ir–OH/GDY-2 and Cp*Ir–OH/GDY-3, respectively, for the FA dehydrogenation in a 3 M FA aqueous solution at 363 K. Figure S17 (Supporting Information) shows that the TOF value of Cp*Ir–OH/GDY is somewhat decreased from 970 to 850 h^{-1} when the Ir loading is increased from 7.59 to 15.36 wt%. This phenomenon could be caused by the fact that as the Ir loading is increased a small number of the Cp*Ir sites may be buried within the GDY structure and inaccessible for catalysis, which makes the calculated TOF value (based on the total Ir loading) lower than the real activity. Unfortunately, the attempts to further decrease the Ir loading of Cp*Ir–OH/GDY was not successful, because when too small amount of the Ir(III) precursor (which acts as an oxidant during the GDY formation process) was added in the preparation the HEB monomer was polymerized only to low-polymerization degree GDY, which is difficult to be isolated from the solution. Nevertheless, the current results demonstrate that i) the total loading of Ir in Cp*Ir–OH/GDY can be modified by changing the amount of precursor in the preparation process and ii) a significant number of the Cp*Ir sites in Cp*Ir–OH/GDY are active for the catalysis of FA dehydrogenation at least with the Ir loading up to 15.36 wt%.

The influence of the FA concentration on the initial TOF of Cp*Ir–OH/GDY for FA dehydrogenation is illustrated in Figure 4c; and Figure S18 (Supporting Information). A volcano relationship between the initial TOF and the FA concentration was observed. The initial TOF reached the maximum value of 850 h^{-1} in a 3.0 M FA aqueous solution. Then the activity decreased with further increase of the FA concentration, owing to the drop of the water concentration as the water concentration plays an essential role in the catalytic FA dehydrogenation.[15] Next, the dehydrogenation of FA was carried out at various pH values (Figure 4d; and Figure S19, Supporting Information) in an aqueous solution (adjusted by the ratio of FA/HCOONa). The catalytic performances of Ir/GDY, Cp*Ir–Cl/GDY, and Cp*Ir–OH/GDY showed remarkable improvement with an increase in pH. Cp*Ir–Cl/GDY and Cp*Ir–OH/GDY demonstrated a much better FA dehydrogenation performance than their precursors, $[Cp*IrCl_2]_2$ and $[Cp*Ir(H_2O)_3]$ (SO_4), at all tested pH conditions (Figure S20, Supporting Information). To our delight, Cp*Ir–OH/GDY displayed a TOF of 2170 h^{-1} at pH 3.9 and 363 K, corresponding to a mass activity of 1726 mmol g^{-1} h^{-1}, while the TOFs of 22–800 h^{-1} were reported over the past few years for the single-atom catalysts supported on carbon materials in FA dehydrogenation at 371–398 K (Table S3, Supporting Information).[16]

In addition, the initial TOFs of all three as-prepared catalysts were further measured at various temperatures to construct the Arrhenius plot (Figure 4e; and Figure S21, Supporting Information). The activation energy for FA dehydrogenation over
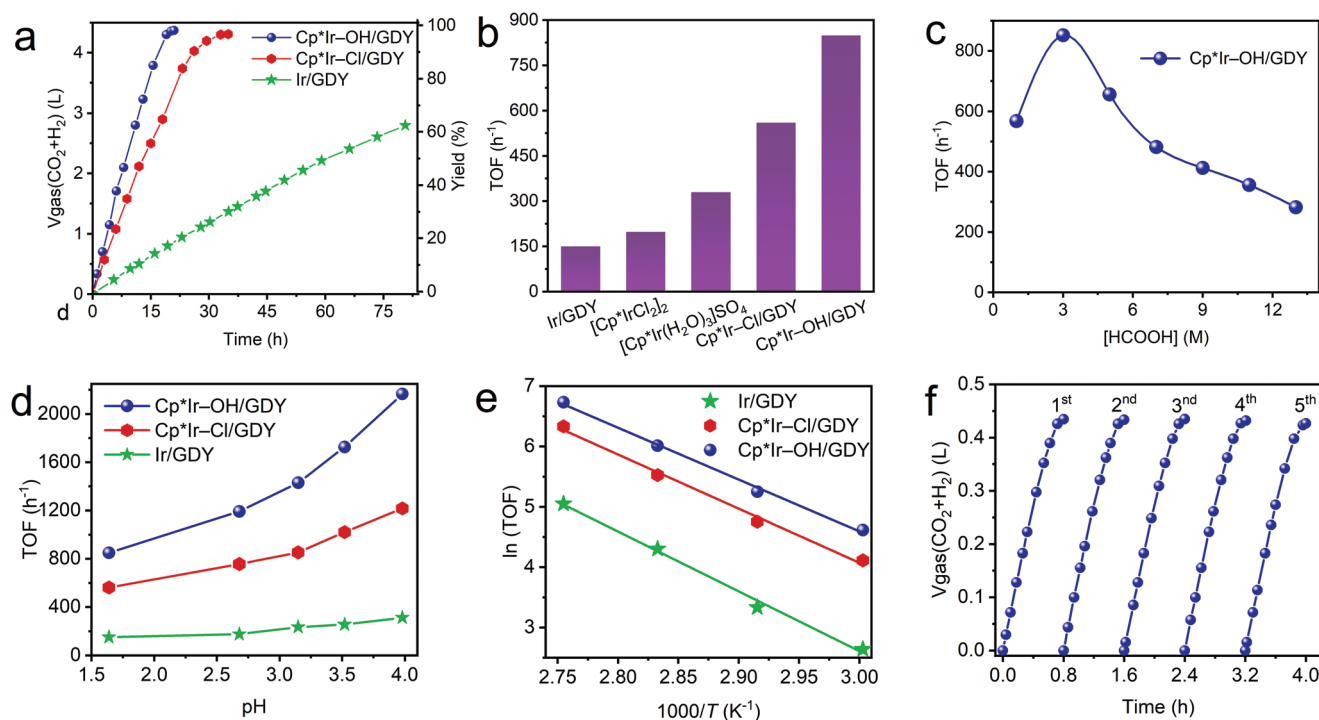
Figure 4. a) Decomposition of FA over different catalysts in a 3 M FA aqueous solution with 10 µmol Ir (total Ir contained in the added catalyst) at 363 K. b) Comparing the TOFs (over initial 30 min) of Ir/GDY, Cp*Ir–Cl/GDY, Cp*Ir–OH/GDY, and related precursors for FA dehydrogenation. c) Plot of initial TOF versus [HCOOH] for Cp*Ir–OH/GDY. d) Effect of pH on TOF for FA dehydrogenation using 1.0 mg of Ir/GDY, Cp*Ir–Cl/GDY, and Cp*Ir–OH/GDY in FA/HCOONa solution (3 M). e) Arrhenius plot for FA dehydrogenation over different catalysts. f) Catalytic performance of Cp*Ir–OH/GDY for FA dehydrogenation during successive rounds of reaction in a 1 M FA aqueous solution with 40 µmol Ir at 363 K.

Cp*Ir–Cl/GDY and Cp*Ir–OH/GDY were calculated to be 74.57 and 71.39 kJ mol^{-1}, respectively, which are lower than that of 82.37 kJ mol^{-1} for Ir/GDY and almost the same as those for the active homogeneous catalysts.[17] For example, the activation energy of [Cp*Ir(4,4'-R$_2$-bpy)(H$_2$O)]SO$_4$ (R = OMe) was reported to be 75.7 kJ mol^{-1} by the Himeda group.[18]

Moreover, the stability of Cp*Ir–OH/GDY was studied by performing successive runs of the reaction (Figure 4f). After five runs, almost 95% of the original activity was preserved. Clearly, Cp*Ir–OH/GDY showed advantages in stability and recyclability over homogeneous iridium catalysts. The XPS, FTIR, XRD, and HAADF STEM measurements were performed over Cp*Ir–OH/GDY after reusability tests. Figure S22 (Supporting Information) shows that there is no notable change in the C 1s and Ir 4f XPS spectra of Cp*Ir–OH/GDY after reusability tests. In the FTIR spectrum of Cp*Ir–OH/GDY after reusability tests (Figure S23a, Supporting Information), the characteristic peaks at 1450, 1380, and 1029 cm^{-1} for the Cp* ring were maintained, suggesting the stability of the Cp* ring on the Ir center during the reaction. Besides, there is no considerable change in the XRD pattern (Figure S23b, Supporting Information), and especially no characteristic peaks of Ir particles after reusability tests, indicating no crystalline Ir particles formed during 5 rounds of FA dehydrogenation. Atomically dispersed Ir centers on GDY were observed by HAADF STEM analysis (Figure S24, Supporting Information) after the reusability test of Cp*Ir–OH/GDY. These results suggest that the single Ir atoms of SHOCs on GDY have not agglomerated during the catalytic reaction.

2.8. Mechanistic Investigation

FA dehydrogenation catalyzed by Cp*Ir type catalysts generally proceeds through three steps (**Figure 5**a):[11d] i) formation of a formate-coordinating intermediate, ii) release of CO$_2$ by β-hydride elimination to generate an Ir–H species, and iii) production of H$_2$ from the reaction of Ir–H and a proton. With the understanding of the overall reaction, we performed in situ FTIR measurements to further investigate the influence of the Cp* ligand on the elementary reaction steps of FA dehydrogenation. First, a catalyst was placed on the top plate of an attenuated total reflectance kit, and the background was acquired. Then the 3.0 M FA aqueous solution was injected on top of the catalyst layer at room temperature and the spectral changes were recorded. Figure 5b shows the representative results using Cp*Ir–OH/GDY as a catalyst together with the FTIR spectra of standard samples of FA and sodium formate. FA in the aqueous solution displayed four distinct bands at 1710, 1635, 1392, and 1187 cm^{-1}, which are assigned to the stretching vibrations of C=O and C–O, and the deformation vibration of O–H. By contrast, only two broad bands were observed at 1580 and 1352 cm^{-1} for the aqueous sodium formate, corresponding to the stretching vibrations of C=O. For the FA dehydrogenation reaction catalyzed by Cp*Ir-OH/GDY, two sets of bands were observed at $t = 1$ min after mixing the catalyst with the FA aqueous solution. One set of bands at 1710, 1635, 1392, and 1187 cm^{-1} are assigned to free FA in the solution, and the other set of bands at 1558 and 1344 cm^{-1}
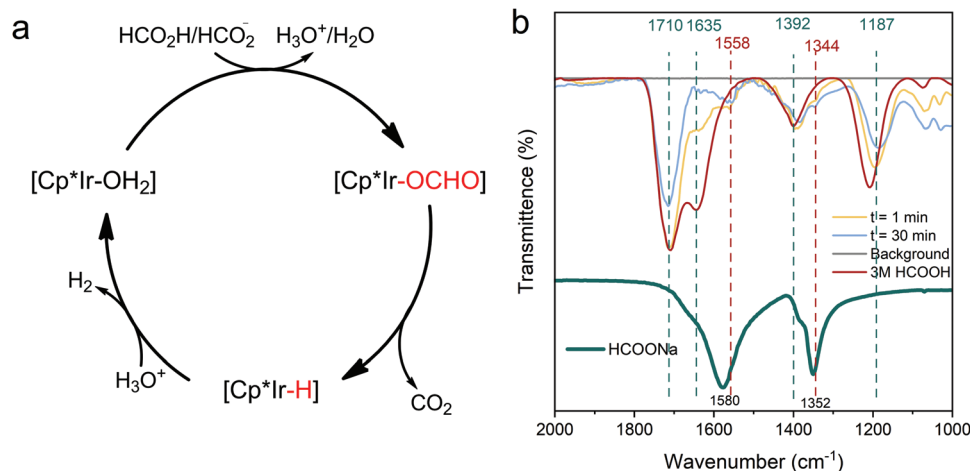
Figure 5. a) Catalytic cycle of Cp*Ir type catalysts for FA dehydrogenation. b) In situ FTIR spectra of Cp*Ir–OH/GDY after being treated with 3 M HCOOH for 1 and 30 min, together with FTIR spectra of HCOOH and HCOONa aqueous solutions.

are similar in shape to the FTIR spectrum of formate but red-shifted by tens of wavenumbers, which are assigned to the adsorbed formate species (HCOO*) binding to the Ir center. After the reaction for 30 min at room temperature, the bands of FA apparently attenuated while the bands of HCOO* species remained almost unchanged. Thus, the HCOO* species is regarded as the resting state in the Cp*Ir–OH/GDY-catalyzed FA dehydrogenation, and in other words, the rate-determining step is the β-hydride elimination reaction (HCOO* → CO$_2$ + H*). Similar results were also observed for Cp*Ir–Cl/GDY and Ir/GDY (Figure S25, Supporting Information).

Furthermore, we studied the deuterium kinetic isotope effect (KIE) to investigate the rate-determining step of the dehydrogenation reaction of FA catalyzed by Ir/GDY, Cp*Ir–Cl/GDY, and Cp*Ir–OH/GDY. The results are summarized in Table S4 (Supporting Information). For all three catalysts, when FA or H$_2$O was replaced by deuterated reagent, the reaction rate significantly decreased compared with that observed for the reaction carried out in 3.0 M FA/H$_2$O solution. A similar KIE trend was observed for all three catalysts. Taking Cp*Ir–OH/GDY for instance, the KIE values are 1.5, 2.5, and 3.3 in the mixed HCOOH/D$_2$O, DCOOD/H$_2$O, and DCOOD/D$_2$O, respectively. The KIE values are 1.6, 2.4, and 3.2 for Ir/GDY and 1.4, 2.3, and 3.1 for Cp*Ir–Cl/GDY. Note that the deuterium in the carboxylic acid, but not the C−D of FA, is able to exchange with the hydrogen of H$_2$O. Apparently, the C−D bond of deuterated FA should display a more pronounced KIE than the O−D bonds of deuterated carboxylic acid and D$_2$O on the reaction rate. Therefore, under test conditions (pH 1.6), the β-hydride elimination, which involves C−H/C−D bond cleavage and Ir−H/Ir−D bond formation, is designated as the rate-determining step, while water is involved in the rate-limiting step most likely via H-bonding networks. Since the rates of FA dehydrogenation for Cp*Ir–Cl/GDY and Cp*Ir–OH/GDY are higher than the rate for Ir/GDY, we deduce that the Cp* ligand on the Ir center could accelerate the rate of the β-hydride elimination step.

DFT calculations were carried out to study the rate-limiting β-hydride elimination step on both Ir/GDY and Cp*Ir/GDY. As shown in **Figure 6**, the decomposition of HCOOH to HCOO* and H* on Ir/GDY is highly exothermic by 0.65 eV. HCOO* is adsorbed in a bidentate form which suggests a strong interaction between HCOO and the Ir site. The further decomposition of HCOO* is uphill by 0.54 eV with a barrier of 1.15 eV. At the transition state, the molecule has rotated to a monodentate form with the H atom pointing to Ir. Therefore, the high barrier is due to the strong interaction between Ir and HCOO*. Owing to the coordination of Cp*, the Ir of Cp*Ir/GDY is not capable of simultaneously adsorbing HCOO* and H*. Even solely adsorbing HCOO* can only be in a monodentate form. Therefore, we suppose that H$^+$ is directly transferred to the solvent as the solvated proton. Then, the first decomposition step of HCOOH on Cp*Ir/GDY is downhill by 0.04 eV. The further decomposition of HCOO* is downhill by 0.63 eV with a kinetic barrier of 1.00 eV, which is 0.15 eV lower than those on Ir/GDY. Therefore, Cp*Ir/GDY is more active for the decomposition of HCOOH. This can be attributed to the weakened interaction between HCOO* and Ir by the Cp* ligand, which lowers the rotation barrier of HCOO*.
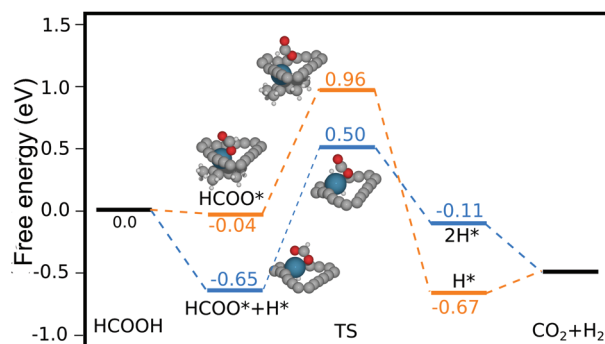

Figure 6. Free energy profiles of FA dehydrogenation catalyzed by Ir/GDY and Cp*Ir/GDY.

3. Conclusion

In summary, we developed a facile and mild method to synthesize single-site heterogenous organometallic Ir catalysts embedded on GDY, namely Cp*Ir–Cl/GDY and Cp*Ir–OH/GDY, and proved the advantages of our strategy of structural and electronic manipulation beyond the carbon support in comparison with the SAC Ir/GDY. The structures of Ir/GDY, Cp*Ir–Cl/GDY, and Cp*Ir–OH/GDY were characterized by XPS and EXAFS. XANES analysis and DFT calculations demonstrated that the oxidation state of Ir in Cp*Ir–L/GDY was higher than that in Ir/GDY, most probably because the negatively charged strong electron-donating ligands Cp*/Cl⁻/HO⁻ increase the energy level of d-electrons of Ir and thus favor the back-bonding from Ir to the coordinated triple bonds in the GDY matrix. With FA dehydrogenation as a proof-of-principle experiment, the results showed that Cp*Ir–OH/GDY displayed a 5-fold increase in activity compared to Ir/GDY. As evidenced by the KIE and in situ FTIR studies, the β-hydride elimination reaction is the rate-limiting step for FA dehydrogenation. Both experimental results and DFT calculations support that the introduction of the electron-donating Cp* ligand on the Ir center accelerates the β-hydride elimination reaction. This example for embedding organometallic complexes directly on the GDY via strong metal-support coordinate bonds provides a way to design more diverse SHOCs on carbon materials for other type of reactions.

Supporting Information

Supporting Information is available from the Wiley Online Library or from the author.

Conflict of Interest

The authors declare no conflict of interest.

Data Availability Statement

The data that support the findings of this study are available in the supplementary material of this article.

[1] S. Ji, Y. Chen, X. Wang, Z. Zhang, D. Wang, Y. Li, *Chem. Rev.* **2020**, *120*, 11900.

[2] a) Y. Chen, R. Gao, S. Ji, H. Li, K. Tang, P. Jiang, H. Hu, Z. Zhang, H. Hao, Q. Qu, X. Liang, W. Chen, J. Dong, D. Wang, Y. Li, *Angew. Chem., Int. Ed.* **2021**, *60*, 3212; b) H. Fei, J. Dong, Y. Feng, C. S. Allen, C. Wan, B. Volosskiy, M. Li, Z. Zhao, Y. Wang, H. Sun, P. An, W. Chen, Z. Guo, C. Lee, D. Chen, I. Shakir, M. Liu, T. Hu, Y. Li, A. I. Kirkland, X. Duan, Y. Huang, *Nat. Catal.* **2018**, *1*, 63.

[3] a) V. Georgakilas, M. Otyepka, A. B. Bourlinos, V. Chandra, N. Kim, K. C. Kemp, P. Hobza, R. Zboril, K. S. Kim, *Chem. Rev.* **2012**, *112*, 6156; b) J. Wang, X. Huang, S. Xi, J. M. Lee, C. Wang, Y. Du, X. Wang, *Angew. Chem., Int. Ed.* **2019**, *58*, 13532; c) K. Yuan, D. Lutzenkirchen-Hecht, L. Li, L. Shuai, Y. Li, R. Cao, M. Qiu, X. Zhuang, M. K. H. Leung, Y. Chen, U. Scherf, *J. Am. Chem. Soc.* **2020**, *142*, 2404; d) J. Zhang, Y. Zhao, C. Chen, Y. C. Huang, C. L. Dong, C. J. Chen, R. S. Liu, C. Wang, K. Yan, Y. Li, G. Wang, *J. Am. Chem. Soc.* **2019**, *141*, 20118; e) T. Zheng, K. Jiang, N. Ta, Y. Hu, J. Zeng, J. Liu, H. Wang, *Joule* **2019**, *3*, 265.

[4] Y. Cai, J. Fu, Y. Zhou, Y. C. Chang, Q. Min, J. J. Zhu, Y. Lin, W. Zhu, *Nat. Commun.* **2021**, *12*, 586.

[5] a) Y. Wu, Z. Jiang, X. Lu, Y. Liang, H. Wang, *Nature* **2019**, *575*, 639; b) X. Zhang, Z. Wu, X. Zhang, L. Li, Y. Li, H. Xu, X. Li, X. Yu, Z. Zhang, Y. Liang, H. Wang, *Nat. Commun.* **2017**, *8*, 14675.

[6] a) M. R. Axet, J. Durand, M. Gouygou, P. Serp, *Adv. Organomet. Chem.* **2019**, *71*, 53; b) M. Blanco, P. Álvarez, C. Blanco, M. V. Jiménez, J. Fernández-Tornos, J. J. Pérez-Torrente, L. A. Oro, R. Menéndez, *Carbon* **2015**, *83*, 21; c) P. Garrido-Barros, C. Gimbert-Surinach, D. Moonshiram, A. Picon, P. Monge, V. S. Batista, A. Llobet, *J. Am. Chem. Soc.* **2017**, *139*, 12907; d) M. Hu, Z. Yao, X. Wang, *Ind. Eng. Chem. Res.* **2017**, *56*, 3477; e) B. I. Kharisov, O. V. Kharissova, A. V. Dimas, I. G. De La Fuente, Y. P. Méndez, *J. Coord. Chem.* **2016**, *69*, 1125; f) R.-X. Li, X.-T. Ren, M.-Y. Tang, M.-X. Chen, G.-B. Huang, C.-H. Fang, T. Liu, Z.-H. Feng, Y.-B. Yin, Y.-M. Guo, S.-K. Mei, J. Yan, *Appl. Catal., B* **2018**, *224*, 772; g) S. Ruiz-Botella, E. Peris, *ChemCatChem* **2018**, *10*, 1874.

[7] a) C. Coperet, A. Comas-Vives, M. P. Conley, D. P. Estes, A. Fedorov, V. Mougel, H. Nagae, F. Nunez-Zarur, P. A. Zhizhko, *Chem. Rev.* **2016**, *116*, 323; b) M. M. Stalzer, M. Delferro, T. J. Marks, *Catal. Lett.* **2014**, *145*, 3; c) R. J. Witzke, A. Chapovetsky, M. P. Conley, D. M. Kaphan, M. Delferro, *ACS Catal.* **2020**, *10*, 11822; d) J. Liu, *ACS Catal.* **2016**, *7*, 34; e) A. Wang, J. Li, T. Zhang, *Nat. Rev. Chem.* **2018**, *2*, 65; f) J. M. Thomas, R. Raja, D. W. Lewis, *Angew. Chem., Int. Ed.* **2005**, *44*, 6456; g) M. K. Samantaray, V. D'Elia, E. Pump, L. Falivene, M. Harb, S. Ould Chikh, L. Cavallo, J. M. Basset, *Chem. Rev.* **2020**, *120*, 734.

[8] a) G. Li, Y. Li, H. Liu, Y. Guo, Y. Li, D. Zhu, *Chem. Commun.* **2010**, *46*, 3256; b) J. Li, Y. Xiong, Z. Xie, X. Gao, J. Zhou, C. Yin, L. Tong, C. Chen, Z. Liu, J. Zhang, *ACS Appl. Mater. Interfaces* **2019**, *11*, 2734; c) R. Matsuoka, R. Sakamoto, K. Hoshiko, S. Sasaki, H. Masunaga, K. Nagashio, H. Nishihara, *J. Am. Chem. Soc.* **2017**, *139*, 3145; d) R. Sakamoto, N. Fukui, H. Maeda, R. Matsuoka, R. Toyoda, H. Nishihara, *Adv. Mater.* **2019**, *31*, 1804211; e) C. Xie, X. Hu, Z. Guan, X. Li, F. Zhao, Y. Song, Y. Li, X. Li, N. Wang, C. Huang, *Angew. Chem., Int. Ed.* **2020**, *59*, 13542; f) J. Zhou, J. Li, Z. Liu, J. Zhang, *Adv. Mater.* **2019**, *31*, 1803758.

[9] a) L. Hui, Y. Xue, H. Yu, Y. Liu, Y. Fang, C. Xing, B. Huang, Y. Li, *J. Am. Chem. Soc.* **2019**, *141*, 10677; b) X. Liu, Z. Wang, Y. Tian, J. Zhao, *J. Phys. Chem. C* **2020**, *124*, 3722; c) Y. Xue, B. Huang, Y. Yi, Y. Guo, Z. Zuo, Y. Li, Z. Jia, H. Liu, Y. Li, *Nat. Commun.* **2018**, *9*, 1460; d) H. Yu, Y. Xue, B. Huang, L. Hui, C. Zhang, Y. Fang, Y. Liu, Y. Zhao, Y. Li, H. Liu, Y. Li, *iScience* **2019**, *11*, 31.

[10] a) W. Rong, H. Zou, W. Zang, S. Xi, S. Wei, B. Long, J. Hu, Y. Ji, L. Duan, *Angew. Chem., Int. Ed.* **2021**, *60*, 466; b) H. Zou, W. Rong, S. Wei, Y. Ji, L. Duan, *Proc. Natl. Acad. Sci. USA* **2020**, *117*, 29462.

[11] a) D. Mellmann, P. Sponholz, H. Junge, M. Beller, *Chem. Soc. Rev.* **2016**, *45*, 3954; b) K. Sordakis, C. Tang, L. K. Vogt, H. Junge, P. J. Dyson, M. Beller, G. Laurenczy, *Chem. Rev.* **2018**, *118*, 372; c) Q. Sun, N. Wang, Q. Xu, J. Yu, *Adv. Mater.* **2020**, *32*, 2001818; d) W. H. Wang, Y. Himeda, J. T. Muckerman, G. F. Manbeck, E. Fujita, *Chem. Rev.* **2015**, *115*, 12936; e) H. Zhong, M. Iguchi, M. Chatterjee, Y. Himeda, Q. Xu, H. Kawanami, *Adv. Sustainable Syst.* **2018**, *2*, 1700161; f) W. Ye, H. Huang, W. Zou, Y. Ge, R. Lu, S. Zhang, *ACS Appl. Mater. Interfaces* **2021**, *13*, 34258.

[12] Z. Li, Y. Chen, S. Ji, Y. Tang, W. Chen, A. Li, J. Zhao, Y. Xiong, Y. Wu, Y. Gong, T. Yao, W. Liu, L. Zheng, J. Dong, Y. Wang, Z. Zhuang, W. Xing, C. T. He, C. Peng, W. C. Cheong, Q. Li, M. Zhang, Z. Chen, N. Fu, X. Gao, W. Zhu, J. Wan, J. Zhang, L. Gu, S. Wei, et al., *Nat. Chem.* **2020**, *12*, 764.

[13] a) M. Peuckert, F. P. Coenen, H. P. Bonzel, *Electrochim. Acta* **1984**, *29*, 1305; b) R. B. Shalvoy, P. J. Reucroft, B. H. Davis, *J. Catal.* **1979**, *56*, 336.

[14] W. Tang, E. Sanville, G. Henkelman, *J. Phys.: Condens. Matter* **2009**, *21*, 084201.

[15] S. Zhang, O. Metin, D. Su, S. Sun, *Angew. Chem., Int. Ed.* **2013**, *52*, 3681.

[16] a) D. A. Bulushev, M. Zacharska, A. S. Lisitsyn, O. Y. Podyacheva, F. S. Hage, Q. M. Ramasse, U. Bangert, L. G. Bulusheva, *ACS Catal.* **2016**, *6*, 3442; b) D. A. Bulushev, M. Zacharska, E. V. Shlyakhova, A. L. Chuvilin, Y. Guo, S. Beloshapkin, A. V. Okotrub, L. G. Bulusheva, *ACS Catal.* **2015**, *6*, 681; c) X. Li, A. E. Surkus, J. Rabeah, M. Anwar, S. Dastigir, H. Junge, A. Bruckner, M. Beller, *Angew. Chem., Int. Ed.* **2020**, *59*, 15849; d) Y. Leng, S. Du, G. Feng, X. Sang, P. Jiang, H. Li, D. Wang, *ACS Appl. Mater. Interfaces* **2020**, *12*, 474; e) M. D. Marcinkowski, J. Liu, C. J. Murphy, M. L. Liriano, N. A. Wasio, F. R. Lucci, M. Flytzani-Stephanopoulos, E. C. H. Sykes, *ACS Catal.* **2016**, *7*, 413; f) O. Y. Podyacheva, D. A. Bulushev, A. N. Suboch, D. A. Svintsitskiy, A. S. Lisitsyn, E. Modin, A. Chuvilin, E. Y. Gerasimov, V. I. Sobolev, V. N. Parmon, *ChemSusChem* **2018**, *11*, 3724.

[17] a) J. F. Hull, Y. Himeda, W. H. Wang, B. Hashiguchi, R. Periana, D. J. Szalda, J. T. Muckerman, E. Fujita, *Nat. Chem.* **2012**, *4*, 383; b) H. Liu, W. H. Wang, H. Xiong, A. Nijamudheen, M. Z. Ertem, M. Wang, L. Duan, *Inorg. Chem.* **2021**, *60*, 3410.

[18] W. H. Wang, S. Xu, Y. Manaka, Y. Suna, H. Kambayashi, J. T. Muckerman, E. Fujita, Y. Himeda, *ChemSusChem* **2014**, *7*, 1976.